Journal of Volcanology and Geothermal Research 418 (2021) 107322

Contents lists available at ScienceDirect

Journal of Volcanology and Geothermal Research

journal homepage: www.elsevier.com/locate/jvolgeores

Earthquake location and detection modeling for a future seafloor observatory along Mayotte's volcanic ridge

Chastity Aiken [a,*], Jean-Marie Saurel [b], Océane Foix [a]

[a] Ifremer, REM-GM-LAD, Plouzané 29280, France
[b] Institut de Physique du Globe de Paris (IPGP), Paris, France

ARTICLE INFO

Article history:
Received 9 March 2021
Received in revised form 21 May 2021
Accepted 14 June 2021
Available online 17 June 2021

Keywords:
Seafloor observatory
Modeling
Location
Detection
Earthquakes
Volcanic system

ABSTRACT

The volcano-seismic crisis afflicting Mayotte since May 2018 has motivated France-based seismologists to consider the installment of a permanent seafloor observatory with one or more seismometers for monitoring surfacing magma and the associated seismicity. In general, deploying a seismometer offshore is known to improve earthquake location – particular in depth – and lower magnitude detection. However, how true are these claims for Mayotte when a land-based seismic network already exists? To address this, we investigate location and detection performance when deploying permanent seismometers offshore Mayotte. We modeled location and detection performance using both real and synthetic data in different network configurations. We found that, in the case of Mayotte, only longitude error is significantly reduced by adding seismometers offshore, perhaps due to the North-South configuration of the land network. Moreover, the size of the Mayotte volcano monitoring area, which spans depths and distances up to 50 km for both, prevents accurate location and detection performance with less than 2 permanent seismometers offshore. Therefore, we would need at least 2 cabled seismometers to monitor this volcanic system, i.e. locate and detect events in real-time. Overall, our modeling suggests that a one-side land network can perform relatively well by itself in location (errors <5 km) and detection (magnitude >1.3) so long as the seismicity occurs at epicentral distances and depths <20 km. However, beyond this distance, one or more seafloor seismometers would be needed to improve location and detection performance.
© 2021 The Authors. Published by Elsevier B.V. This is an open access article under the CC BY-NC-ND license (http://creativecommons.org/licenses/by-nc-nd/4.0/).

1. Introduction

Mayotte – a set of small islands lying just northwest of Madagascar and part of the Comoros archipelago – has been overwhelmed with seismic activity along its submarine volcano ridge since May 2018, and this seismic activity continues even until today, 21 May 2021 (Fig. 1). A new volcano edifice was discovered a year after the crisis begin, located ~50 km east of Petite Terre (Feuillet et al., 2019a, 2019b, 2021). The new volcano edifice is located at the eastern part of a N130° alignment of volcanic edifices. Lemoine et al. (2020) proposed that volcanic activity occurred as a result of fracturing, diking, and finally magma drainage. This is consistent with the transtensional environment of the Comoros archipelago accommodating the extension between the Somalian plate and the Rovuma microplate in the East African Rift System (Famin et al., 2020; Stamps et al., 2020).

Since the beginning of the Mayotte volcano crisis, several land-based seismometers have been permanently installed (Saurel et al., 2019, 2021) and ocean bottom seismometers have been regularly recovered and deployed during several oceanographic campaigns (MAYOBS 1 to MAYOBS 15; May 2019 to October 2020). These onshore and offshore deployments facilitated the detection and location of ≥4000 earthquakes, having magnitude as small as 1. Magnitude ≥3 events have been detected and located almost completely (Saurel et al., 2019, 2021). In addition to earthquakes, the OBS deployments have afforded opportunities to characterize very long period tremors (Lemoine et al., 2020; Feuillet et al., 2019a, 2019b, 2021) and to detect drumbeat earthquakes, volcanic tremors, volcano-tectonic events, and hydro-acoustic explosions that have not all been observable on the land network.

Overall, seismic data collected during the MAYOBS oceanographic campaigns have highlighted that there are 2 seismically active areas offshore over a distance of ~50 km from Petite Terre, Mayotte's smaller island. The fact that the seismicity is spread over such a large distance, offshore and east of Mayotte, makes it seemingly difficult to monitor Mayotte's volcano ridge using only land-based stations. Mayotte's real-time monitoring land-based network is predominantly a one-sided station geometry (e.g., Fig. 1). Such a network configuration at continent-ocean transitions is well-known to affect location accuracy in the direction perpendicular to its coast (Braunmiller et al., 1997). A seafloor observatory can improve seismicity relocation and lower detection thresholds (Tréhu et al., 2018). Therefore, to monitor this active

* Corresponding author at: Ifremer, Centre de Bretagne, REM-GM-LAD, 1625 Route de Sainte Anne, 29280 Plouzané, France.
E-mail address: chastity.aiken@ifremer.fr (C. Aiken).

https://doi.org/10.1016/j.jvolgeores.2021.107322
0377-0273/© 2021 The Authors. Published by Elsevier B.V. This is an open access article under the CC BY-NC-ND license (http://creativecommons.org/licenses/by-nc-nd/4.0/).

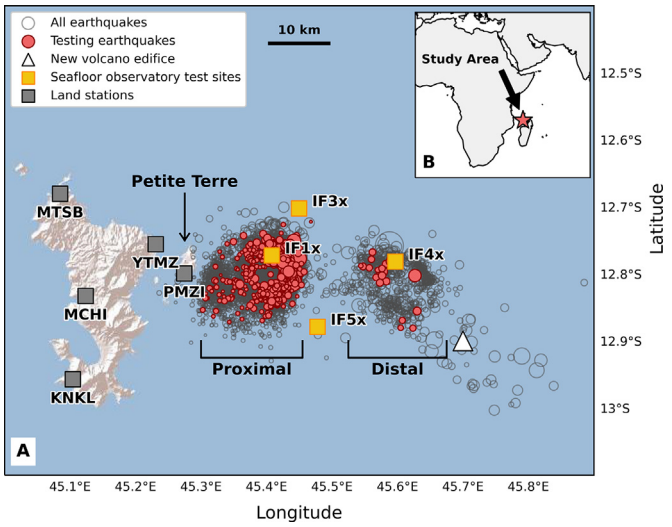


Fig. 1. Map view of Mayotte's earthquakes and seafloor testing site locations. A) More than 4000 manually relocated earthquakes using offshore deployments are shown in gray, and 564 earthquakes used in this study are shown in red. There are 2 seismic swarms, which we call the Proximal and Distal swarms. The new volcano edifice (white triangle) is located ~50 km away from Petite Terre, Mayotte's smaller island. The yellow squares represent potential seafloor observatory sites, where OBS have been deployed. Select land stations used in this study are displayed as gray squares. B) Mayotte's location northwest of Madagascar (red star).

submarine volcano ridge, we now seek to add a permanent seafloor observatory.

Seafloor observatories offer possibilities to collect a wide range of geological, chemical, physical, and biological data for investigating processes that drive the dynamic earth-ocean system over a broad spectrum of oceanic environments. Thus, deploying seismometers offshore can impact overall how earth-ocean processes are studied, and the ability to study these processes from an interdisciplinary angle is priceless. A number of seafloor observatories already exist in the world and have proven to provide a wealth of data. For instance, the DONET (Dense Ocean floor Network system for Earthquakes and Tsunamis) (Kaneda et al., 2009; Kawaguchi et al., 2010) and SNET (Seafloor observation Network for Earthquakes and Tsunamis) (NIED, 2019) are real-time submarine cabled observatories located offshore Japan. The NEPTUNE (North East Pacific Time-series Underwater Networked Experiments) observatory offshore Vancouver Island, Canada and the many observatories created under the Ocean Observatories Initiatives (OOI) off the northwestern coast of the U.S.A. (e.g. Favali et al., 2015) are other examples of seafloor observatory monitoring of volcanoes such as Axial Seamount. In general, seafloor observatories can operate as their own distinct network or as a supplement to land-based networks. They typically collect a range of data that is transmitted in real-time or near real-time back to land either by way of a cable or remote transmission. These seafloor observatories have facilitated the collection of a multitude of data to study interactions among geological, chemical, physical, and biological processes that drive the dynamic earth-ocean system over a broad spectrum of oceanic environments. In the case of Axial Seamount, the seafloor observatory has led to a better understanding of the volcano, with eruption forecast updated in real-time.

In this study, we investigate the possibility of installing a permanent seafloor observatory that would monitor Mayotte's volcanic plumbing system. This seafloor observatory would include the deployment of one or more seismometers for monitoring seismic activity along the ridge, among other types of scientific instrumentation (for geodesy, geochemistry, biology). However, seafloor observatories require major development plans, and even what is considered an affordable solution for the installment can be seen as costly. Because the entire length of the Mayotte volcano ridge has been activated during the crisis (over a distance of ~50 km), we ask – what is the optimal location for a seismometer in a seafloor observatory to monitor seismicity offshore Mayotte, and what can be gained by installing seismometers offshore, supplementing the land-based network for a reasonable cost? To answer these questions, we perform a number of tests that illustrate how seismometers in a seafloor observatory at different sites (Section 2) will influence location performance of earthquakes (Section 3) and also how they might perform in terms of magnitude detectability (Section 4). Our goal is to demonstrate what can be gained by deploying one or more permanent seismometers offshore Mayotte, while assessing the value of endeavoring to create a seismic seafloor observatory where a land-based seismic network already exists.

2. Seafloor sites

During the many MAYOBS cruises, 4–16 ocean-bottom seismometers (OBS) were recovered and re-deployed often at the same sites. By deploying at the same sites, we maintained a consistent seismic network for evaluating the earthquake locations across the deployments. For evaluating the best seafloor observatory site, we chose 4 OBS sites, which are IF1*x*, IF3*x*, IF4*x*, and IF5*x*, where *x* corresponds to a specific MAYOBS deployment, i.e. A, B, C and so on (Fig. 1). The IF1*x* site is close to Petite Terre, within ~10 km and can possibly be cabled. It is located near the center of the Proximal swarm, which is ideal for monitoring volcano activity that might place the people of Mayotte at risk. IF3*x* is located north and east of the Proximal swarm and can also be perceivably cabled. The location of IF3*x* permits monitoring of the Proximal swarm area without being susceptible to volcanic activity and offers an additional station north of the ridge and east of the Proximal swarm. At present, there is only one station north of the ridge on Glorieuse Island at regional distance. The IF4*x* site is located closer to the new volcano edifice, positioned near the central portion of the ridge on the northern side. It is located almost directly on top of the Distal swarm and, at this distance from Petite Terre, would require mooring to keep installation costs low. The IF5*x* site is located on the southern edge of the ridge and, like IF3*x*, is still capable of monitoring the Proximal swarm area and increases azimuthal coverage without apparent risk to instrumentation. Given the distance of the IF5*x* site to Petite Terre, it might need to be moored to avoid exorbitant costs. In general, the choice of a site being cable or moored will depend on which sites perform best, keeping in mind a target budget of around 10 M €.

3. Location performance

In this section, we describe the data sets and methods applied, as well as investigate how Mayotte's land network performs compared to the land network complemented with a potential real-time seismometer in a seafloor observatory offshore Mayotte. At present, earthquakes detected offshore Mayotte have been located at depths between 20 and 50 km, and we lack shallow earthquake data. Because shallow events are important for understanding potential hazards to Mayotte's people, we use theoretical travel times from shallow synthetic sources in addition to the real earthquake data. The synthetic travel times provide a deeper understanding of the full capability of a seismometer in a seafloor observatory when locating offshore activity at various depths. Below, we present our location performance testing data, methods, and results.

3.1. Real data tests

Hand-picked phase arrivals from earthquakes recorded by OBS between 17 May 2019 and 8 June 2019 were used to analyze network location performance. We chose this deployment period because it contains the most relocated earthquakes with phases on all 4 seafloor

observatory test sites (Fig. 1) that also have a wide magnitude range ($1 < M < 4.7$) (Fig. S1). From this deployment period, we selected 564 earthquakes that had been accurately located by analysts using both land stations and at least 7 OBS (Fig. S2). While there are several land stations installed on Mayotte, not all are reliable. Therefore, to maintain testing conformity across different earthquakes, we selected 5 local land stations with the largest number of hand-picked phases across all OBS deployment periods (Fig. 1), as those land stations are obviously the most reliable for recording phases needed for earthquake location. Additional information about all stations used in this study is available in Table S1.

We compare a 5-station land network performance by itself to the performance of a 5-station land network with 1 real-time potential seafloor seismometer site. With 4 seafloor testing sites, there are a total of 5 possible testing cases: land stations only, land stations + IF1*x*, land stations + IF3*x*, and so on. Thus, for testing conformity, we required that each of the 564 earthquakes have ≥1 phase (*P*- and/or *S*-wave) picked on 5 local land stations and ≥1 phase on each of the 4 OBS testing sites, i.e. IF1*x*, IF3*x*, etc. All other earthquakes were excluded from the analysis.

While the 5 chosen land stations provide the most phases and are seemingly the most reliable, at times data are lost or have bad quality. For instance, station KNKL tends to have high residuals, and when locating events, the 'ADofal' velocity model (Saurel et al., 2021) is known to perform badly for that station (Feuillet et al., 2019a, 2019b, 2021). While KNKL high residuals are likely counter-balanced when multiple OBS are used to locate an event, this station might have a more significant impact on the location when there is only 1 seafloor seismometer. Station MCHI is located at a school, and unfortunately, sometimes the power is cut to the instrument during school vacation for multiple weeks. In addition, station YTMZ is an accelerometer, and earthquake phases might not be visible on this station when the event is of small magnitude. Thus, to account for potential data loss or undetected events, we perform a jack-knife resampling (a linear approximation of bootstrapping) by dropping each land station once (5 possible drops +1 no-drop case = 6 station drop cases) when relocating each event. This results in 564 earthquakes × 5 testing cases × 6 station drop cases for a total of 16,920 relocations using hand-picked phases.

For each of the 16,920 relocations, we used the *NonLinLoc* algorithm (Lomax et al., 2014). Phase arrival uncertainties, as assigned by analysts, were included in the algorithm input when available. For the relocation tests, we use the same velocity model that was established from earthquake detection and location during the MAYOBS 1 cruise (hereafter, the MAYOBS velocity model; Table S2), as well as the same *NonLinLoc* configuration, which has 1-km grid spacing (e.g. Feuillet et al., 2019a, 2019b, 2021). Both are consistent with on-going earthquake monitoring within the REVOSIMA (REseau de surveillance Volcanologique et SIsmologique de MAyotte) framework of French institutions that monitor on-going Mayotte submarine volcanism. Fig. 2 is an example of results from the different testing cases (i.e. seafloor site, land station drop) for a single earthquake. From this example, it is clear that the land network by itself performs poorly compared to when a seafloor site is added, and where that seafloor site exists influences the location performance. In Section 3.3, we present and discuss the location results for all earthquakes and the different network configurations.

3.2. Synthetic data tests

We simulate sources at depths similar to that of the real data, at depths 20–50 km as well as in shallow depths (<20 km). This allows us to evaluate the quality of the synthetic results against those from the real data, which can further help us evaluate shallow synthetic earthquake location performance where no real data exists. The synthetic sources are located along the entire ridge at multiple depths (Fig. 3). Sources are located on nodes of a 3D gridded volume with

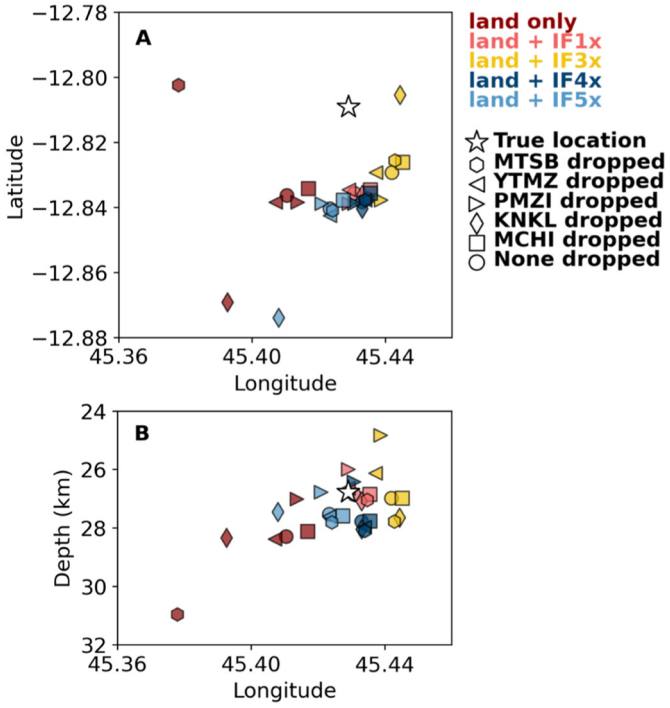


Fig. 2. Relocation results from the different testing cases applied to a single earthquake (star). The earthquake has magnitude 2.1 and occurred on 2 June 2019 06 h40. A) Locations in map view. B) Locations in cross-section. Color represents the seismic network configuration, i.e. which seafloor site is used in the relocation or not at all, and symbols demonstrate the different bootstrap tests for land station data that might be lost.

longitude and latitude boundaries of 45.3° and 45.76° and −12.95° and −12.69°, respectively, spaced every 3.3 km and depths between 0 and 50 km, spaced every 2 km. As the seafloor bottom increases in depth away from the islands of Mayotte (eastward), synthetics sources that would be above the seafloor (MAYOBS1; Feuillet et al., 2021) were excluded from the analysis (Fig. 3B). These criteria resulted in 3501 potential sources along the Mayotte volcano ridge.

For each synthetic source, we predict the P- and S-wave travel times at each of the stations using the *TauP* program within the *obspy* Python module. Because the *TauP* program requires velocity profiles down to the center of the Earth, we supplement the MAYOBS velocity model with the *ak135* global velocity model at depths ≥77.5 km (Tables S2–S3). We note that certain focal mechanisms may not result in visible phase arrivals at our stations. However, the focal mechanisms so far for offshore Mayotte exhibit a wide range (e.g. Cesca et al., 2020), and the structures generating the earthquakes are not well understood at present. Thus, for the purpose of this study, we do not exclude any phase travel times with respect to focal mechanism.

We require that each synthetic source have at least 1 observable phase (either up-going or down-going) on each of the stations in Table S1, similar to the real data analysis. Forty-five sources do not fit these criteria and were excluded from the analysis. These sources were located at 2-km depth at all latitudes west of 45.42°, at the shallowest depth above the Proximal swarm (Fig. 3). Therefore, no synthetic sources at depths <4 km where included in the analysis. For those sources, no phase was recorded at site IF4*x*, a result of the events' shallowness and the seafloor topography. Excluding events with no P- or S-wave arrivals at IF4*x* leaves 3456 synthetic sources for analysis.

Because our velocity model is not perfect, modeled time arrivals would have errors in real data. We then added random noise to the theoretical travel times (e.g., Table 1) for more realistic times. The added random picking errors are Gaussian distributed with zero mean and 0.1 s standard deviation for P-arrivals and 0.2 s for S-arrivals, similar to travel time residuals in the real data

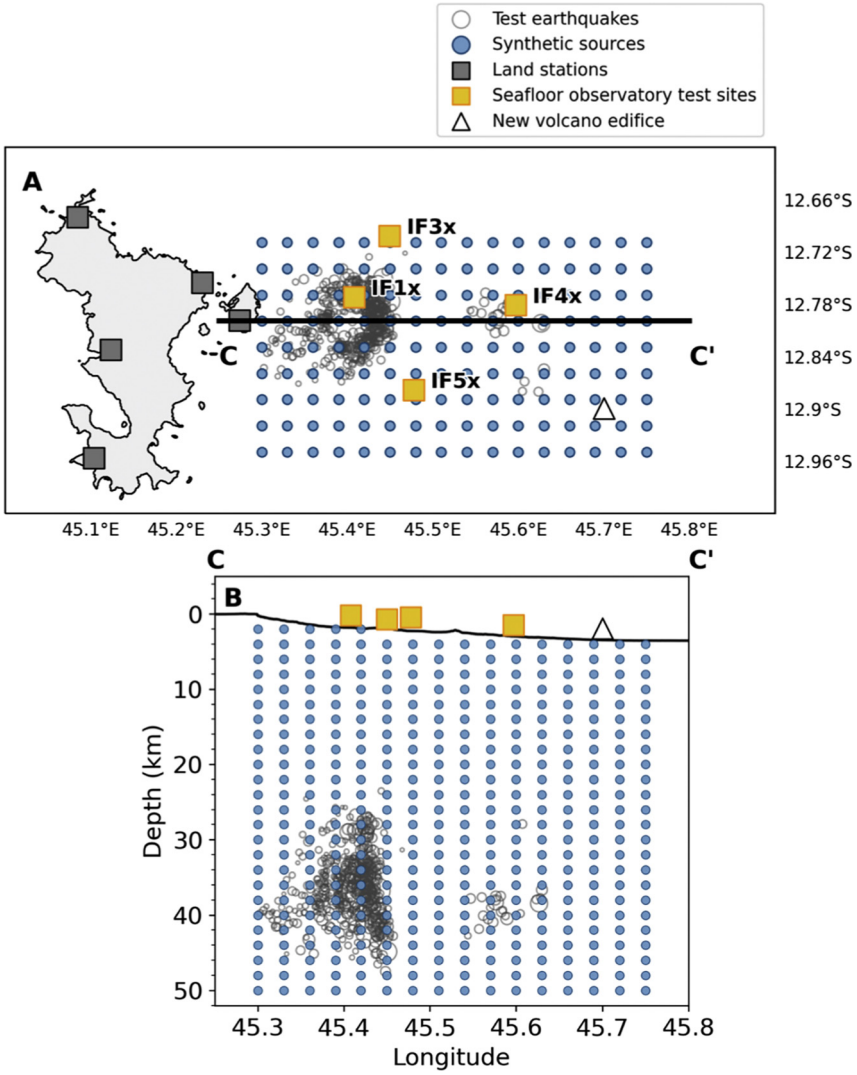


Fig. 3. Synthetic sources for testing location performance. A) Map view, similar to Fig. 1, except the colored circles represent synthetic sources and gray circles are testing earthquakes described in Section 3.1. The new volcano edifice is marked as a white triangle. B) Transect C-C′ profile shown in A. The black line represents the deepening seafloor topography eastward from Mayotte. There are 3501 synthetic sources.

(Foix et al., 2020, 2021). Using the modeled travel times, we then constructed *NonLinLoc* input files for locating the synthetic sources similar to the real data tests, i.e. locating each source with the land stations only or land stations +1 seafloor site while also performing a small bootstrapping by dropping each land station once. This resulted in 3456 sources × 5 testing cases × 6 station drop cases for a total of 103,680 synthetic source relocations.

Table 1
Computed values for a synthetic event located at 45.42°E, 12.80°S and 26 km deep.

Station	Angular	Predicted travel times		Randomly added error	
	Distance (°)	P-wave (s)	S-wave (s)	P-wave (s)	S-wave (s)
MTSB	0.348	7.76	12.89	+0.01	−0.12
YTMZ	0.190	5.63	9.35	+0.01	+0.31
PMZI	0.142	5.14	8.53	−0.04	−0.07
MCHI	0.291	6.91	11.48	−0.26	−0.43
KNKL	0.346	7.73	12.83	−0.19	+0.24
IF1*x*	0.030	4.02	6.68	+0.01	−0.18
IF3*x*	0.095	4.34	7.21	−0.00	−0.03
IF4*x*	0.173	4.85	8.05	−0.05	−0.15
IF5*x*	0.111	4.24	7.03	−0.10	−0.23

3.3. Location performance results

3.3.1. Deep seismicity

We first compare the outcomes of the 16,920 real earthquake relocation tests to their true locations. A true location is one that has been determined from phases picked on all available land stations and at least 7 OBS (e.g. Saurel et al., 2019, 2021). When real earthquakes are relocated with few phases, a smaller network, and different configurations, they tend to be located more south and west of their true locations (Fig. 4A), independent of the seafloor site used for the relocation. By itself, the land network performs the worst in terms of longitude, with errors on average of 5 km, most likely due to the land network's one-sided nature (Fig. 1). Surprisingly, the land network performs on average quite well with depth.

Adding a seafloor observatory seismometer to the 5-station land network offers little to no improvement in latitude, but seafloor sites do tend to reduce errors in longitude and at least increase precision for depth (Fig. 4A). Sites IF3*x* and IF4*x* – located on the north side of the ridge – perform best in reducing longitudinal error, with an average accuracy of ~1 km from the true location. However, the longitude precision of site IF4*x* is 1.5 times better than site IF3*x*. Site IF1*x*, which is located in the middle of the Proximal swarm closest to the islands,

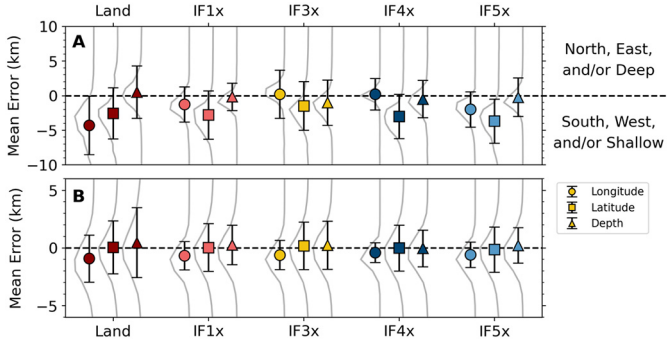


Fig. 4. Mean errors for deep events (≥20 km) relocated in the 5 different testing scenarios. The gray lines represent 1-km binned histograms of the errors with symbols and bars representing means and standard deviations of longitude, latitude, and depth errors for A) real data and B) synthetic data.

and site IF5*x*, located on the Proximal swarm's southeastern edge, also reduce longitude error but not as well as IF3*x* and IF4*x*. While there is a general improvement in location, eastward of the different network configurations, i.e. further from the land network, the location errors can still be a little poor particularly in longitude (Fig. S3A). Overall, longitudinal error is reduced by 3–4 km among all possible seafloor seismometer sites when compared to the land network performance. However, it should be considered that the real data error distributions might be biased by the earthquake locations, i.e. the majority of earthquakes are concentrated near Petite Terre (Fig. 1).

To better assess how the different seafloor sites might perform with deep earthquakes occurring along the entire Mayotte volcano ridge, we created synthetic sources and relocated them similar to the real data (Section 3.2). Like the real sources, synthetic sources at similar depths (≥20 km) also tend to be located more westerly of their true location with an average accuracy of 1 km or less and depth precision increasing when a seafloor site is used in the relocation (Fig. 4B). In contrast to the real data, the deep synthetic sources appear to be accurately located in latitude and depth on average (Fig. 4B), although slightly more deep than real events. The synthetic event relocation errors are about half the size of the real data. This is likely because we used a similar velocity model to predict the phase arrival times and to perform the relocation (see Section 3.2), albeit randomized Gaussian errors had been added to the theoretical travel times prior to relocation (e.g., Table 1).

In cross-sectional view (Fig. 5), location errors appear to be both systematic and random, depending on the testing scenario. However, there is an alignment between relocated earthquakes (Fig. 5A) and relocated synthetic sources (Fig. 5B). For instance, the land stations only scenario has clear systematic errors in the real and synthetic data. Unfortunately, we do not have many real observations of deep events beneath the volcano in this dataset due to new volcano edifice being located ~50 km away from the land network. However, irrespective of the seafloor seismometer testing site scenario, both real and synthetic deep events located closest to the new volcano edifice are poorly located, even when using site IF4*x* which performs the best (Fig. 4). Site IF4*x* has the greatest precision in both the real and synthetic tests for deep events, i.e. having a smaller range of longitudinal error (~1–2 km) compared to the other seafloor sites or the land network alone (Fig. 4). Site IF4*x* is equally likely to perform well because its position makes the seismic network have a wider vision of the lengthy earthquake source region (Fig. 1).

Overall, the deep synthetic data set reproduces quite well the location error distributions observed from deep real data. Therefore, we can arguably and safely use synthetics to assess how different network configurations might perform for shallow events.

3.3.2. Shallow seismicity

Because shallow events have not yet been detected in the real data, we generated synthetic phase arrivals to test shallow event (<20 km) location performance when adding a seafloor seismometer (Section 3.2). Similar to deep sources (≥20 km), shallow synthetic sources tend to be located more westerly of their true locations (Fig. 6A), and the different network configurations exhibit similar performance in latitude and depth location, whether or not a seafloor seismometer site exists. However, the land network does have a wider range of error over a network that contains a seafloor site. As with deeper events, shallow event location is mostly improved in the longitude with the addition of a seafloor seismometer over using the land network alone. Sites IF1x and IF5x have better precision in their error, particularly in longitude and depth, compared to sites IF3*x* and IF4*x* for deep events (Fig. 4). Therefore, if the goal is to monitor shallow earthquake activity, site IF1x or IF5x would be a better choice. On the other hand, shallow sources near the new volcano edifice are poorly located and, unlike like deeper events, tend to be located more deeply than their 'true' location (Fig. 6B, Fig. S3). However, site IF4*x* reduces errors the best for events occurring on the most eastern part of the volcano ridge.

Perhaps what is most notable is that depths of shallow events overall have a much larger error range (Fig. 6A) than deeper events (Fig. 4). This is expected given that it is difficult to model shallow crustal velocity layers and the length scale over which seismicity can occur. That is, seismic waves do not "see" shallow, thin layers very well. The synthetic location errors (Fig. 6A) are relatively small compared to the real data (Fig. 4A), and as stated previously, these small variations may be related to how we predicted and treated theoretical phase arrival times. Nevertheless, shallow sources are located similarly to that of the real and synthetic deep sources. Thus, we can conclude that gains in shallow seismicity will likely be similar at least in longitude, i.e. 3–4 km. In depth, we can assume that on average shallow events will be well-located, but the shallow source depths will in general have a slightly wider range of error (Fig. 6A) than what has been observed for their deep counterparts (Fig. 4).

3.3.3. Effect of velocity model

Mainly longitude error is significantly reduced when adding a seismometer offshore Mayotte, despite where the seismometer site might be located, and the error is reduced by only 3–4 km (e.g., Figs. 4, 6). We suspect the low gains in longitude might be due to the fact that we currently have a velocity model for locating earthquakes offshore Mayotte, due to the many MAYOBS oceanographic campaigns. That is to say, if we had installed a seismometer offshore to monitor the volcano before having improved the velocity model with the OBS deployments, would we have seen larger gains in location performance than we do with the MAYOBS velocity model? To test this, we relocated earthquakes with a standard *ak135* global velocity model (Kennett et al., 1995).

As expected, the *ak135* global velocity model tends to perform worse than the improved MAYOBS velocity model, but mostly in longitude and depth for deeper events and only slightly (Fig. 7). While the MAYOBS model tends to place deep events more deeply (Fig. 4), the *ak135* model tends to place them shallower. However, even with the *ak135* global model, deep events are still located more westerly and/or southerly of their true location, as seen in both real and synthetic tests (Fig. 7A–B). Considering the case of having no a priori knowledge of the velocity model offshore Mayotte, a seismometer placed offshore would have reduced longitude errors by ~5 km or less compared to the land network alone for deep events (Fig. 7A–B). However, deep events would not improve in latitude or depth accuracy, only precision, similar to when using the MAYOBS velocity model (Fig. 4).

Shallow events appear to be easily locatable, at least horizontally, whether or not a seafloor seismometer exists and despite whether or not the velocity model is known (Fig. 7C). However, for shallow sources, the land network performs quite badly in depth when using the *ak135* velocity model, placing the events more deeply. Because of this, adding a seismometer offshore promotes larger gains in depth for shallow sources, i.e. ~3 km reduction in mean depth error over the land network

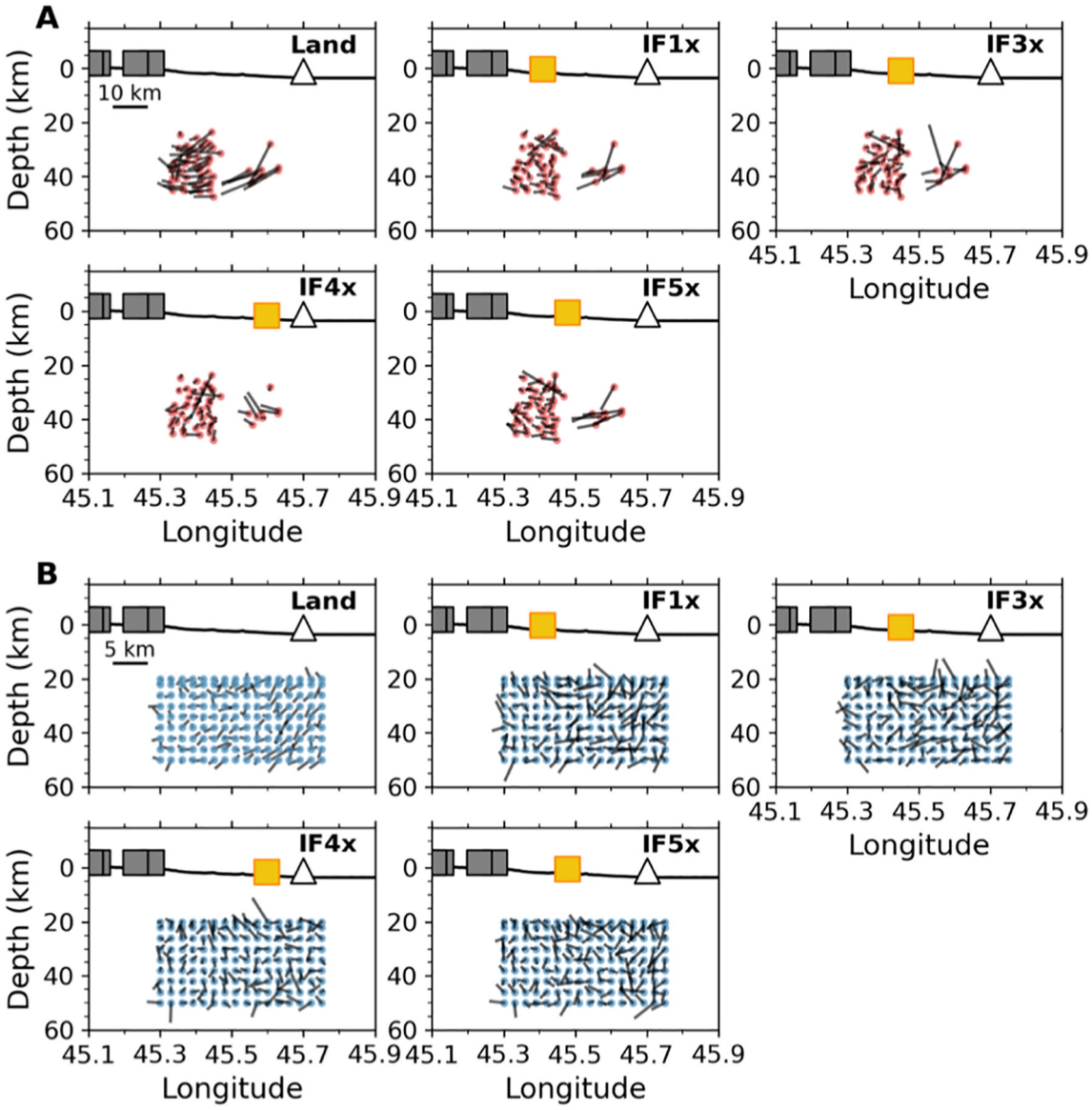


Fig. 5. Cross-section views of deep events (≥20 km) relocated in the 5 different testing scenarios. We do not illustrate location performance in latitude as the performance is roughly the same whether or not a seafloor site is used for relocation (Fig. 4). Relocations of A) 50 real earthquakes and B) 144 synthetic sources with true locations +/− 2 km from profile C-C′ in Fig. 3. The panels represent the different testing scenarios, as noted in the top right of each panel. Triangles represent the new volcano edifice, gray squares are land stations, and yellow squares are the different seafloor testing sites. Circles represent true locations (real = red; synthetic = blue), and lines point to the average across all locations made by dropping each land station once for the sources shown. Location errors in B have been exaggerated by 2 to better demonstrate location error trends. Scales for error shown in 'Land' panels.

alone in the synthetic case. Thus, depths of shallow events would appear to improve if we installed a seafloor seismometer and had no a priori knowledge of a velocity model for the region. As the synthetics appear to have mean errors half that of the real data, at least for deeper events (Fig. 4), we could assume that the depth gains for shallow events would be about an average 6 km if we had no velocity model for the region. However, the precision would not be as good as that observed with a refined velocity model. In general, this velocity model test indicates that most of the location error differences are due to static bias between the velocity models, i.e. the results are independent of the model used. It demonstrates that good network coverage and geometry is necessary to reduce location errors, independently from the velocity model.

3.3.4. Adding a second seafloor site

Here, we assess location performance in the case that we install 2 permanent seafloor observatory seismometers. With 4 potential seafloor sites (Section 2), there are 6 possible seafloor site pairs that can be used to locate earthquakes in combination with the 5-station land network, e.g. IF1*x*-IF3*x*, IF1*x*-IF4*x*, IF1*x*-IF5*x*, etc. For these 6 station pairs, we construct the NLL files as described previously and relocate each source for each station pair. With 564 earthquakes and 3501 synthetic sources, this results in 23,688 relocations using hand-picked phases and 145,152 relocations using synthetic phases. Fig. 8 demonstrates results from the 2-station location performance tests.

In general, adding a second seafloor site for real and synthetic sources slightly improves the accuracy and increases the precision of source location over a single station. However, on average each seafloor site pair performs roughly the same. While there is no dramatic difference in their average location performance, the precision of seafloor site pair IF3*x*-IF5*x* indicates that this station pair is the best performer. Seafloor site pair IF3*x*-IF5*x* are very near the center of the Mayotte volcano ridge, to the north and south, respectively. Their positions are such

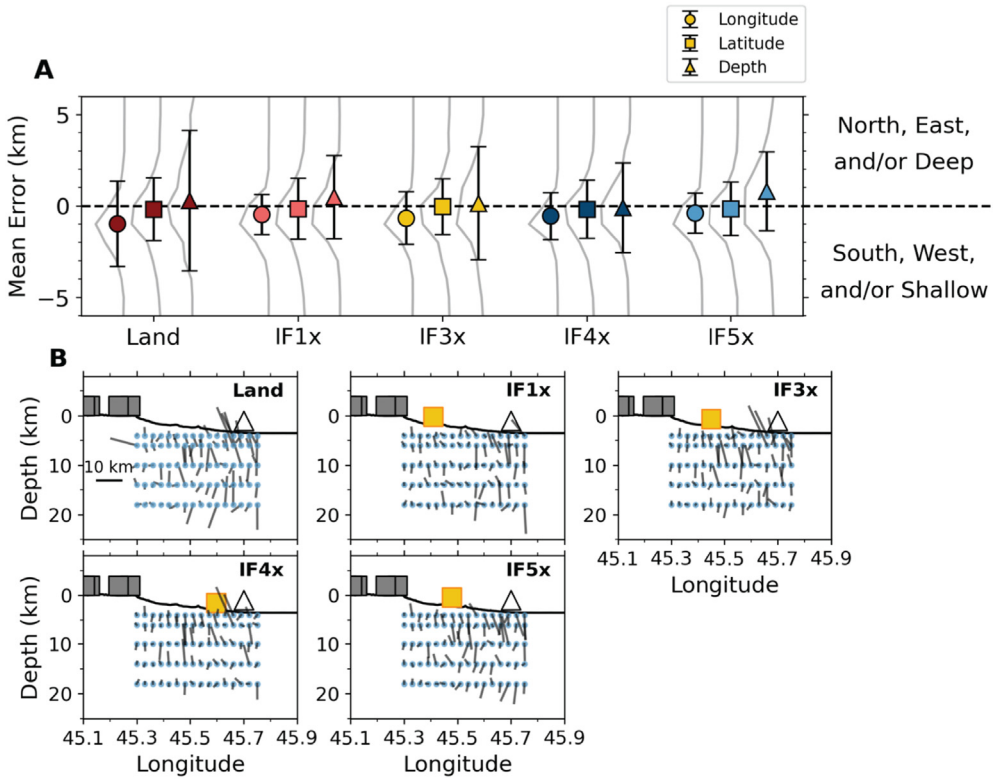


Fig. 6. Mean errors and cross-section views for shallow events (<20 km) relocated in the 5 different testing scenarios. A) Error distributions for synthetic shallow events and B) cross-sectional view of 80 selected shallow synthetic sources (to enhance comprehension) along profile C-C′ in Fig. 3. Symbols and notations are the same as in Figs. 4 and 5, with the exception that location errors have not been exaggerated here.

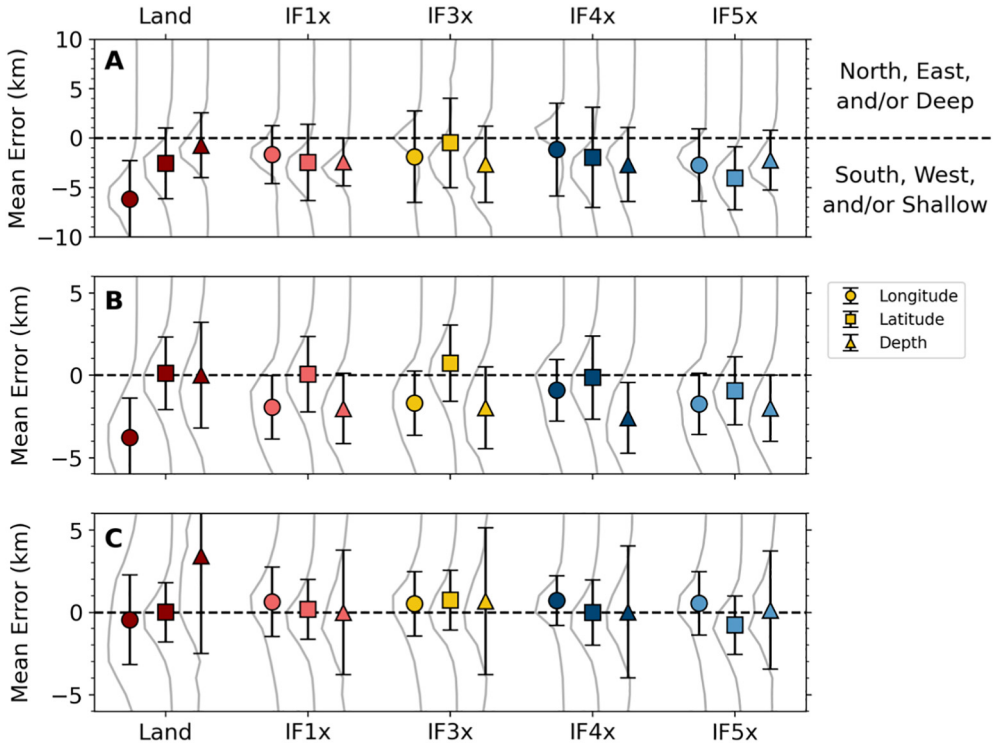


Fig. 7. Mean errors for sources relocated in the 5 different testing scenarios using the *ak135* global velocity model. A) All real earthquakes, which have sources at depths >20 km, B) Deep (≥20 km) synthetic sources, and C) shallow (<20 km) synthetic sources. Symbols and notations are the same as in Fig. 4.

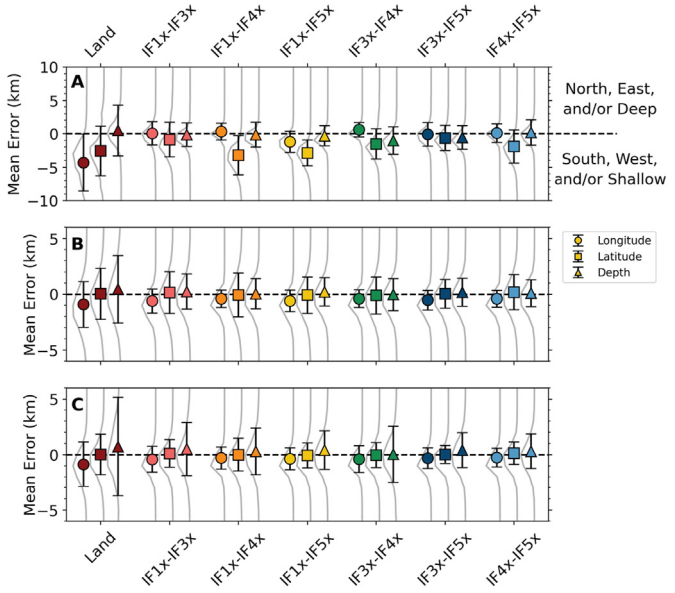


Fig. 8. Mean errors for sources relocated in the 7 different testing scenarios using 2 seafloor sites. A) All real earthquakes, which have sources at depths >20 km, B) Deep (≥20 km) synthetic sources, and C) shallow (<20 km) synthetic sources. Symbols and notations are the same as in Fig. 4.

that they are capable of monitoring both the Proximal swarm closest to Petite Terre and earthquake activity further east toward the new volcano edifice.

4. Magnitude detectability

We know from the series of MAYOBS cruises that the land-based network can detect, at times, down to about magnitude 1, but not consistently. The magnitude 1 events detected by the land-based network tend to occur close to Petite Terre within the Proximal swarm (Fig. S1) and have similar locations to events of higher magnitude. However, these small magnitude events are often not visible with standard network detection filters, are very badly located, at least during the first automatic location, and are therefore overlooked by analysts. Overall, the land network detection threshold is ~M2.0 at nighttime and ~ M2.5 during daytime due to cultural noise levels (Saurel et al., 2021). By adding a permanent seafloor observatory, it is possible we can not only improve their first automatic location but also lower the limit of detectable magnitude. In this section, we estimate the lowest detectable magnitude when using seafloor sites as a supplement to the land network and compare this performance to the 5-station land network monitoring the volcano ridge alone.

4.1. Methods

We roughly follow the method of McNamara et al. (2016) to test the lower limit of detectable magnitude. We update the equations here in our own work, where errors were found in McNamara et al. (2016). We first estimate the frequency-dependent noise levels at individual stations in our proposed seismic network. We determine the noise levels for vertical channels of stations in our proposed network using long-term distributions of power spectral density (PSD) and compute PSD probability density functions (PPSD). For small earthquakes to be detected, the P- and/or S-wave spectral acceleration must exceed long-term median noise levels at frequencies higher than 0.5 Hz, which is a lower limit for cultural and natural noise (McNamara and McNamara and Buland, 2004).

An example of variations in vertical component PPSD during 2019 for land station YTMZ and seafloor observatory test site IF4*x* is shown in Fig. 9. During 2019, the noise levels for YTMZ and IF4*x* are quite high, close to the New High Noise Model (Peterson, 1993). However, of all the stations used in the analysis, these 2 are the quietest with respect to land and seafloor stations. YTMZ's high noise level in the 1–30 Hz band is likely associated with cultural noise at higher frequencies and may be in part related to the vast number of earthquakes recorded during 2019, as the Mayotte volcano crisis was still very active. IF4x's noise curve, with limited PPSD dispersion resembles that of a short-period sensor. Therefore, we assume this station level is limited by its instrumental self-noise. For the seafloor sites, we are considering the installment of Trillium sensors for the seafloor observatory, which have very low self-noise (Fig. 9). Therefore, for seafloor sites, we will compare theoretical P and S-wave amplitudes of earthquakes to a noise curve threshold of 15 dB higher than New Low Noise Model and Trillium Compact theoretical self-noise, which seems to be a reasonable estimate of the performance of such a sensor in an OBS. However, as cultural noise is unavoidable, we compare the observed land station noise levels to theoretical P- and S-wave amplitudes of earthquakes.

To determine the smallest detectable earthquake magnitude, we must compute the M_w detection threshold for different sized sources located along the volcano ridge and compare the theoretical spectral acceleration amplitude to mean noise levels for corresponding stations. We first compute seismic moments M_0 (dyn-cm) for sources having moment magnitudes (M_w) following Kanamori (1977):

$$M_w = 0.667\, log\,_{10} M_0 - 10.7$$

for $0 \le M_w \le 3.6$ with 0.1 spacing, as we know the land network can detect almost completely $M > 3$ (Fig. S1). We estimate their fault dimension r (i.e. crack length in cm) and their corner frequency f_c (Hz) following Brune (1970, 1971):

$$M_0 = 2.29\sigma r^3$$

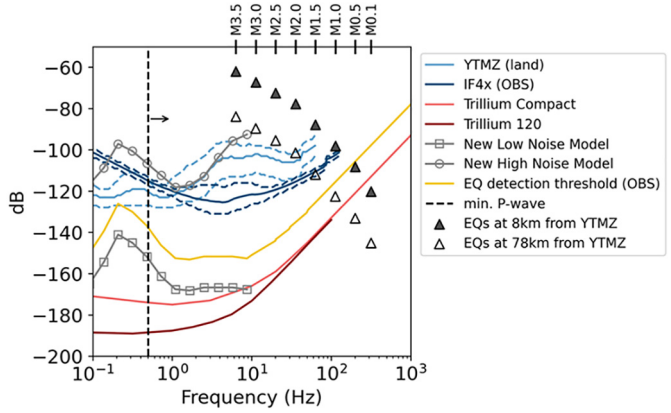


Fig. 9. An example of power spectral density probability density functions (PPSD) and earthquake detection. The PPSDs for 2 instruments, land site YTMZ and OBS site IF4*x*, are compared to the new low and high noise models (Peterson, 1993) and to theoretical self-noise levels of Trillium Compact and Trillium 120 instruments. YTMZ and site IF4*x* have the lowest noise levels among all stations depicted in Fig. 1. For YTMZ and IF4*x*, solid lines are median noise levels, and dashed lines represent the 10th and 90th percentiles. Vertical dashed line represents the minimum frequency a detectable P-wave of an earthquake would need to exceed. Theoretical P-wave amplitudes in dB for several magnitudes (triangles) are shown for an earthquake occurring 8 and 78 km away from YTMZ. We use land station individual median noise levels as a detection threshold and 15 dB above the new low noise model and the Trillium Compact for OBS sites. We note that the seismic instrumentation is not expected to record up to 1000 Hz; it is simply a theoretical representation.

$$r = \frac{2.34\beta}{2\pi f_c}$$

where $\sigma = 100$ bars $= 10^8$ dyn cm^{-2} and $\beta = 3.5 \times 10^5$ cm s^{-1}. Then, for each of the ~3500 synthetic source locations depicted in Fig. 3, we calculate the hypocentral distance (Δ) between all source-station pairs. Next, for each magnitude at each location, we calculate the Brune source spectrum over a range of frequencies ($f = 0.01$ to 10^4 Hz) such that:

$$\Omega(\omega) = \frac{\sigma\beta}{\mu}\frac{r}{\Delta}\frac{1}{(\omega^2 + \omega_c^2)}$$

where μ is rigidity (35×10^{10} dyn cm^{-2}), angular frequency $\omega = 2\pi f$, angular corner frequency $\omega_c = 2\pi f_c$ corresponding to each M_0, and Ω is the Brune source spectrum. We estimate the maximum angular frequency ($\omega_m = 2\pi f_m$) as the angular frequency where the difference in the slope change from where the Brune source spectrum is maximum, i.e. flat, and the slope changes more than 1% (Fig. S4). For each magnitude at each location modeled in this way, we then calculate the S-wave maximum amplitude (A_0) due to the Brune source model:

$$A_0 = \frac{M_0\pi}{\rho\beta^3\Delta}\frac{f_m^2 f_c^2}{f_m^2 + f_c^2}$$

where $\rho = 2.9$ g cm^{-3} for oceanic basalt. In this equation, stress drop (σ) and crack length (r) were substituted using the equations above and shear rigidity (μ) was substituted from the shear wave speed equation $\beta = (\mu/\rho)^{1/2}$. We approximate the effect of attenuation on the S-wave amplitude as:

$$A_s = A_0 e^{\frac{-\pi f_m \Delta}{Q\beta}}$$

where $Q \sim 224 f_m^{0.64}$ (McNamara et al., 2016), and A_s is the attenuated S-wave amplitude, i.e. peak ground velocity (PGV), in cm s^{-1}. Because both P- and S-waves of earthquakes are sometimes detected by the Mayotte real-time monitoring software, we also estimate P-wave PGV (A_p) from the modeled Brune A_s using a standard S/P ratio of $A_p = A_s/3$. As station noise levels are computed from the acceleration spectrum, we use a simplified empirical relationship from (Wald et al., 1999) to estimate peak ground acceleration (PGA) from PGV:

$$log_{10}(0.01PGA) = log_{10}PGV + 1$$

where PGV is in cm s^{-1} and PGA is in m s^{-2}, after converting from Gal (1 Gal = 0.01 m s^{-2}). Finally, the P and S-wave PGAs are converted to power (P) in dB with $P = 20\log_{10}(PGA)$ for comparison to station noise levels. Power of each synthetic earthquakes' P- and S-waves are then compared to the station noise levels. An earthquake is detectable if at least 2 seismic stations can see P- or S-waves above their median noise levels. We assess magnitude detectability as if there are 2 seafloor sites in operation because having only 1 seismometer offshore does not meet the 2-station/2-phase requirement. We require 2 seafloor sites because we are assuming a seafloor site has a lower noise level than the land stations. If 2 phases are required on 2 stations, then 2 seafloor sites would "see" an earthquake before a single seafloor site and any station in the land network. Assuming there are 2 seafloor sites, we evaluate detection performance for 7 different testing scenarios of 2 seafloor site combinations.

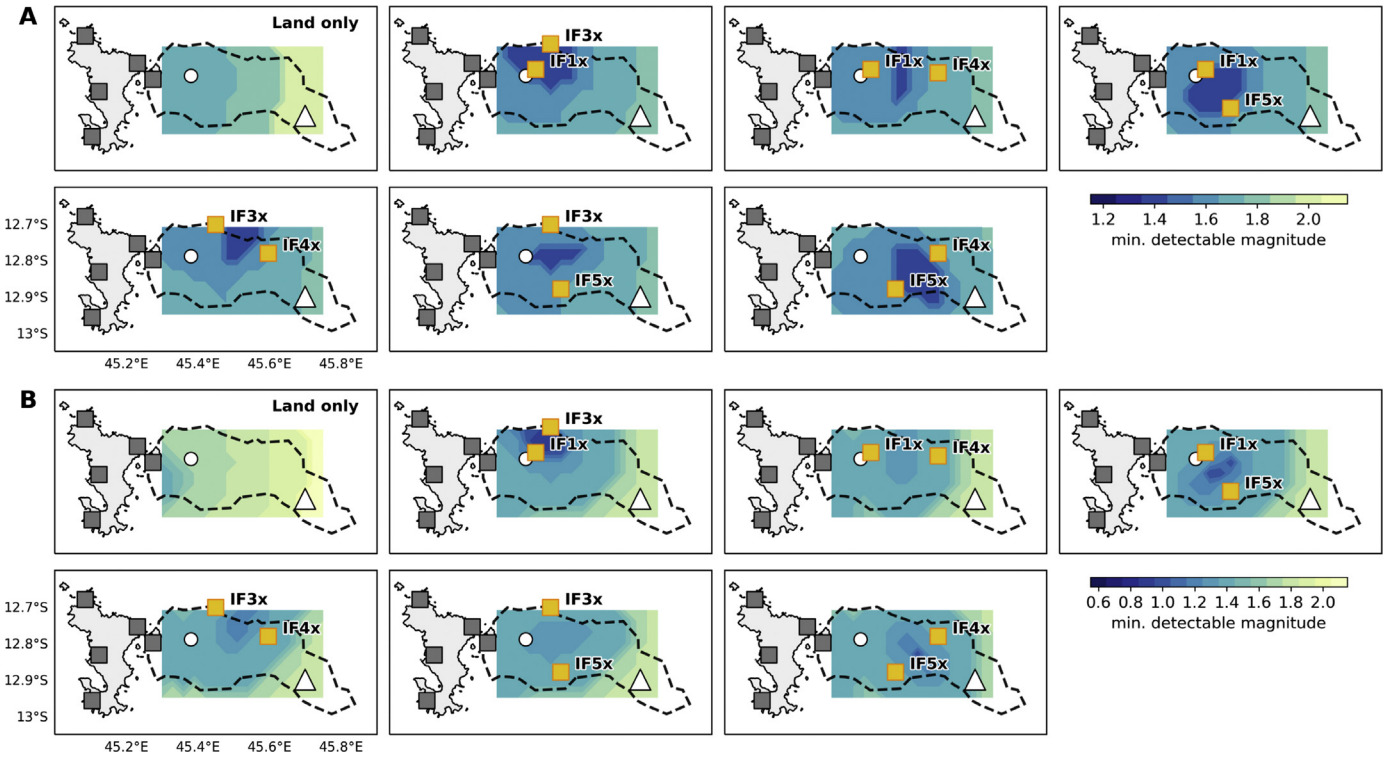


Fig. 10. Lowest detectable magnitude at 2 depths for the 7 different testing scenarios using 2 seafloor sites. A) earthquakes occurring at 24 km depth. B) earthquakes occurring at 4 km depth. Each panel represents a single network configuration, e.g. land stations only, land stations + IF1*x* + IF3*x*, land stations + IF1*x* + IF4*x*, etc. A and B have their own color bar that is shared among all the panels, respectively. The color bar represents the lowest detectable magnitude in each of the configurations. The dashed outlined area is a concave hull of seismicity that has been detected by the land network, e.g. Fig. 1. The white circle marks the horizontal location of a magma reservoir. Other symbols and notation are similar to that of Fig. 1.

4.2. Magnitude detectability results

To effectively monitor the eruptive cycle of the Mayotte's volcanic ridge, we must examine the lowest detectable magnitude at the depth where one of its magma reservoir has been interpreted from geobarometry (Berthod et al., 2020, 2021) and local passive tomography (Foix et al., 2021) and located at ~25 km depth, just east of Petite Terre.

Our earthquake detection modeling indicates that the land network by itself can detect reliably at M ≥ 1.7, at least for events located near or above the magma reservoir near Petite Terre (Figs. 10 and 11). The land network, as expected, performs worse in detection closer to the new volcano edifice (~40 km east). Where seismometers are placed offshore influences the shape and size of the lowest detectable magnitude region horizontally, but this is not the case in depth (Fig. S5). The shape and size of the lower detectable magnitude regions look similar across the different network configurations we tested, at least along profile C-C′ (Fig. 11, Figs. S7–S10). In general, the greatest improvement in magnitude detectability is visible at depths <20 km. In the shallower depths (<20 km), adding two seismometers at sea reduces the lowest detectable magnitude by 0.6 (Fig. S5–S6). For deeper seismicity (≥20 km, where seismicity is observed currently), magnitude detection threshold is reduced by at most 0.3 (Figs. S5–S6). The results suggest that shallow seismicity detection would be improved in certain regions, but not uniformly. However, closer to the magma reservoir, there would be less improvement in magnitude detectability.

Considering the 7 different network configurations and the known location of one of the primary magma reservoirs, having seafloor seismometers at sites IF1*x* and IF5*x* yields one of the wider small magnitude detectable regions horizontally. These sites also reduce the observable magnitude near Mayotte's primary magma chamber, as well as in the primary earthquake region. Therefore, placing seismometers at sites IF1*x* and IF5*x* would be the best choice for monitoring seismicity associated with Mayotte's main magma chamber, e.g. magmatic degassing or new plumbing pathways.

We note that at present the land network can detect completely M ≥ 3 earthquakes (Fig. S1), but the lowest magnitude relocated in the earthquake database is M ~ 1. However, the M1 events are often very badly located with automatic phase picks usually being accurate on 1 station but often badly picked on other stations, i.e. as noise. Therefore, by adding OBS data, the MAYOBS/REVOSIMA seismology team has completely manually picked and relocated earthquakes in the Mayotte region during certain observation periods. Most events have okay first automatic locations by the land network that place them near to where we would expect them. In OBS recording periods, where we have relocated events down to the smallest magnitude using OBS, we have observed a similar lowest magnitude as seen in our detection modeling (Figs. 10 and 11), i.e. the land network can detect events of M ~ 1.7 or higher. In particular, our modeling for the land-network shows results similar to the detection threshold we observe in the real-time monitoring network during night-time (quiet period). Thus, our magnitude threshold estimation is probably good within a degree of 0.5 magnitude uncertainty. Furthermore, we note our detection modeling gives an indication of whether or not an earthquake would be detectable but not if it is "pickable." PGA and PGV typically arrive later than the first arriving phases. Therefore, our conversion of M_w to PGA and PGV cannot tell us if an earthquake's first arrival P- and S-wave phases can be visible to an analyst. Consequently, the actual magnitude thresholds may be slightly higher than what is shown in Figs. 10 and 11, but the relative contours should remain valid.

5. Conclusions

In this study, we simulate the location and detection performance of adding a seafloor observatory offshore Mayotte to monitor its recently active volcano ridge. We conducted several performance tests using both real and synthetic earthquake phase and location data (Section 3.1–3.2) and synthetic magnitude data (Section 4.1) for the land-based seismic network and several offshore sites (Fig. 1).

While it is commonly thought among seismologists that deploying a seismometer offshore a land seismic network improves earthquake locations, especially their depths, we discovered that this claim is not necessarily true, especially when a pretty good local velocity model is available. In general, adding a seafloor seismometer offshore Mayotte improved earthquake location, but the gains are seen mostly in longitude – not in latitude or depth. Overall, adding a seafloor

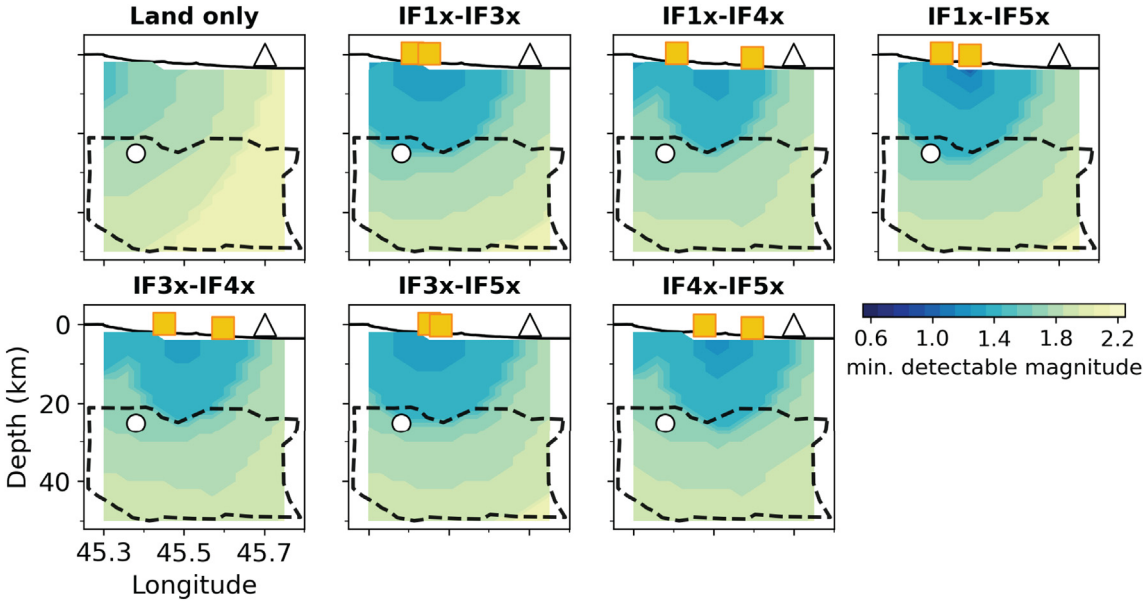


Fig. 11. Lowest detectable magnitude depth cross-sections for the 7 different testing scenarios using 2 seafloor sites. Each panel represents a single network configuration, e.g. land stations only, land stations + IF1*x* + IF3*x*, land stations + IF1*x* + IF4*x*, etc., along profile C-C′ (see Fig. 3). The color bar on the bottom right is shared among all the panels and represents the lowest detectable magnitude in each of the configurations. The dashed outlined area is a concave hull of seismicity that has been detected by the land network. The white circle marks the location of a magma reservoir as determined from Foix et al. (2021). Other symbols and notation are similar to that of Fig. 1.

seismometer offshore Mayotte tends to reduce location error by <5 km, but mostly for those events closest to Petite Terre (Fig. 4–6). To be precise, adding additional offshore sites does not necessarily improve accuracy but does improve precision (Figs. 4, 6, and 8).

The length and depth of the volcanic system offshore Mayotte render the optimal sites for location using one or more seafloor seismometers largely dependent upon what sources have to be monitored. For example, if our goal is to locate well deep events associated with the known magma reservoir activity, then optimal seafloor observatory site choices would be IF3*x* or IF4*x*, with IF4*x* providing better precision. On the other hand, if our goal is to locate well shallow seismicity associated with gas, magma, and/or hydrothermal fluid rising to the surface, indicative of potential eruptive activity, then optimal seafloor observatory site choices would be IF1*x* or IF5*x*. Surprisingly, adding a second seafloor seismometer does not greatly improve location performance (Fig. 8). We attribute the small reduction in location errors, particularly in depth, to the fact that seismometer deployments during MAYOBS campaigns have facilitated an improved velocity model offshore Mayotte. Therefore, earthquake location gains are slightly larger when the velocity model is unknown (Section 3.3.3).

Our location performance tests suggest that a single seismometer is sufficient for earthquake location near Petite Terre, but in terms of magnitude detectability, more than one seismometer offshore is needed to improve event detection threshold. With an offshore seismometer, the noise level is expected to be considerable lower than land based seismometers that are contaminated with cultural noise (e.g., Fig. 9), which can reduce the detectable range. However, we considered that event detection occurs when at least 2 phases (P and/or S waves) are seen by 2 different seismometers. Therefore, to lower the magnitude detection threshold, more than 1 offshore seismometer would be required, contrary to what is observed for earthquake location. If we add 2 permanent seafloor sites offshore Mayotte to monitor earthquake activity, then sites IF1*x* and IF5*x* perform the best both in depth and laterally (Figs. 10 and 11), effectively reducing the detectable magnitude by 0.2–0.5.

In general, our modeling suggests that there is perhaps a distance/depth threshold for when one or more seafloor seismometers adds value to locating earthquakes in real-time monitoring situations when a close land network exists. We observed that at epicentral distances and depths >20 km from the land network (e.g. IF4x) a seafloor seismometer improves event location performance more than a site <20 km from the land network (e.g., Fig. S3). We note, however, that adding one or more seafloor seismometers in general improves earthquake location and detection, even if the gains are small. In the case of detection, if there is only 1 seismometer deployed offshore, then advance detection techniques would likely need to be applied, such as single-station location techniques using back-azimuth or detection on a single instrument using a simple STA/LTA (short-term average/long-term average) method to identify events not meeting the 2 phase/2 seismometer detection threshold.

Based on our models, the reduction in location error (<5 km) and gain in magnitude detectability (0.2–0.5) are both relatively small for Mayotte. A single permanently cabled seismometer (e.g. IF1*x* or IF5x) is obviously not enough to improve magnitude detection threshold offshore Mayotte, but one site is sufficient for earthquake location. However, for optimized location performance, we would likely need a moored instrument further away from Petite Terre, e.g. a seismometer capable of monitoring the full length of the ridge (e.g. IF4*x*). A moored instrument at site IF4*x* would cost roughly the same as a cabled instrument at site IF1*x*, but the moored instrument would not provide real-time capabilities, which is an important criteria for monitoring this volcanic system. The compromise is we should either not purchase a single cabled seismometer or spend enough money to have at least 2 cabled seismometers.

A grant proposal was submitted in June 2020 requesting funding from ANR for 3-seismometer cabled seafloor observatory offshore Mayotte under the acronym of MARMOR (**M**arine **A**dvanced geophysical **R**esearch equipment and **M**ayotte multidisciplinary **O**bservatory for **R**esearch and response). Half of the funding requested in the MARMOR proposal specifically aims to install cabled seismometers at sites IF3*x* and IF5*x*, and one other just south of site IF1*x*. These sites, based on our analysis, perform well individually and should certainly perform well in combination also. Since December 18, 2020, we now know that MARMOR has been accepted and will be funded. Considering the depth and extent of the Mayotte volcanic system and our seismic network performance modeling, we are preparing to deploy 3 seismometers offshore Mayotte. The aim is to reliably improve detection at both shallow and deep depths for the region just east of Petite Terre, which presents the greatest hazard.

Declaration of Competing Interest

The authors declare that they have no known competing financial interests or personal relationships that could have appeared to influence the work reported in this paper.

Acknowledgments

We express our gratitude to all those who contributed to the acquisition of the earthquake data set. Instrument deployment and research oceanographic MAYOBS and Tellus Mayotte cruises were funded by the CNRS (National Scientific Research Agency), MI (Interior Ministry), MOM (Overseas Territory Ministry), MTE (Environment Ministry), MESRI (Higher Education, Research and Innovation Ministry), and MINARM (Armed Forces Ministry). MAYOBS oceanographic campaigns were conducted with the help and collaboration of several French research institutions: Institut de Physique du Globe de Paris (IPGP), BRGM-French geological survey, and Institut Français de Recherche pour l'Exploitation de la Mer (IFREMER). We sincerely appreciate the assistance of Genavir technicians and engineers. We personally thank the crew of R/V Marion Dufresne (TAAF/IFREMER/LDA) and their Captains A. Eyssautier and F. Landreau. We also thank members of the MAYOBS/REVOSIMA (https://www.ipgp.fr/fr/revosima/reseau-de-surveillance-volcanologique-sismologique-de-mayotte) seismology team for the deployment of onshore instrumentation, their hand-picking of earthquake phase arrivals, and their scientific exchanges.

Appendix A. Supplementary data

Supplementary data to this article can be found online at https://doi.org/10.1016/j.jvolgeores.2021.107322.

References

Berthod, C., Médard, E., Bachèlery, P., Gurioli, L., Di Muro, A., Peltier, A., Komorowski, J.C., Benbakkar, M., Devidal, J.-L., Langlade, J., Besson, P., Boudon, G., Rose-Koga, E., Deplus, C., Le Friant, A., Bickert, M., Nowak, S., Thinon, I., Burckel, P., Hidalgo, S., Kaliwoda, M., Jorry, S., Fouquet, Y., Feuillet, N., 2020. The 2018-ongoing Mayotte submarine eruption: magma migration imaged by petrological monitoring. Am. Geophys. Union Fall Meet. Abstract ID V043-03 https://hal.uca.fr/hal-03108840.

Berthod, C., Médard, E., Bachèlery, P., Gurioli, L., Di Muro, A., Peltier, A., Komorowski, J., Benbakkar, M., Devidal, J., Langlade, J., Besson, P., Boudon, G., Rose-Koga, E., Deplus, C., Le Friant, A., Bickert, M., Nowak, S., Thinon, I., Burckel, P., Hidalgo, S., Jorry, S., Fouquet, Y., Feuillet, N., 2021. The 2018-ongoing Mayotte submarine eruption: magma migration imaged by petrological monitoring. Earth Planet. Sci. Lett. Under review (submitted on September 16, 2020).

Braunmiller, J., Leitner, B., Nábělek, Tréhu, A.M., 1997. Location and source parameters of the 19 June 1994 ($M_w = 5.0$) offshore Petrolia, California, earthquake. Bull. Seismol. Soc. Am. 87 (1), 272–276.

Brune, J., 1970. Tectonic stress and the spectra of seismic shear waves from earthquakes. J. Geophys. Res. 75, 4997–5009. https://doi.org/10.1029/JB075i026p04997.

Brune, J., 1971. Correction [to Tectonic stress and the spectra of seismic shear waves from earthquake]. J. Geophys. Res. 76, 5002. https://doi.org/10.1029/JB076i020p05002.

Cesca, S., Letort, J., Razafindrakoto, H.N.T., Heimann, S., Rivalta, E., Isken, M.P., Nikkhoo, M., Passarelli, L., Petersen, G.M., Cotton, F., Dahm, T., 2020. Drainage of a deep magma reservoir near Mayotte inferred from seismicity and deformation. Nat. Geosci. 13, 87–93. https://doi.org/10.1038/s41561-019-0505-5.

Famin, V., Michon, L., Bourhane, A., 2020. The Comoros archipelago: a right-lateral transform boundary between the Somalia and Lwandle plates. Tectonophysics 789, 228539. https://doi.org/10.1016/j.tecto.2020.228539.

Favali, P., Beranzoli, L., De Santis, A., 2015. Seafloor Observatories: A New Vision of the Earth from the Abyss. Springer, Chichester, U.K. 676 pp.

Feuillet, N., Jorry, S., Crawford, W.C., Deplus, C., Thinon, I., Jacques, E., Saurel, J.-M., Lemoine, A., Paquet, F., Daniel, R., Gaillot, A., Satriano, C., Peltier, A., Aiken, C., Foix, O., Kowalski, P., Laurent, A., Beauducel, F., Grandin, R., Ballu, V., Bernard, P., Donval, J.-P., Géli, L., Gomez, J., Pelleau, P., Guyader, V., Rinnert, E., Besançon, S., Bertil, D., Lemarchand, A., Van der Woerd, J., 2019a. Birth of a volcano offshore Mayotte through lithospheric-scale rifting. Am. Geophys. Union Fall Meet. Abstract ID V52D-01 https://ui.adsabs.harvard.edu/abs/2019AGUFM.V52D..01F.

Feuillet, N., Jorry, S., Rinnert, E., Thinon, I., Fouquet, Y., 2019b. MAYOBS. French Oceanographic Cruises https://doi.org/10.18142/291.

Feuillet, N., Jorry, S., Crawford, W.C., Deplus, C., Thinon, I., Jacques, E., Saurel, J.-M., Lemoine, A., Paquet, F., Satriano, C., Aiken, C., Foix, O., Kowalski, P., Laurent, A., Rinnert, E., Cathalot, C., Donval, J.-P., Guyader, V., Gaillot, A., Scalabrin, C., Moreira, M., Peltier, A., Beauducel, F., Grandin, R., Ballu, V., Daniel, R., Pelleau, P., Gomez, J., Besançon, S., Géli, L., Bernard, P., Bachelery, P., Fouquet, Y., Bertil, D., Lemarchand, A., Van der Woerd, J., 2021. Birth of a large volcanic edifice through lithosphere-scale dyking offshore Mayotte (Indian Ocean). Nat. Geosci. https://doi.org/10.31223/X5B89P Under review, pre-print on Eartharxiv.org.

Foix, O., Aiken, C., the MAYOBS/REVOSIMA seismology team, 2020. Offshore Mayotte volcanic plumbing revealed by local passive tomography. Am. Geophys. Union Fall Meet. Abstract ID V043-02 https://agu.confex.com/agu/fm20/meetingapp.cgi/Paper/691041.

Foix, O., Aiken, C., Saurel, J.-M., the MAYOBS/REVOSIMA Seismology Team, Feuillet, N., Jorry, S., Rinnert, E., Thinon, I., 2021. Offshore Mayotte volcanic plumbing revealed by local passive tomography. J. Volcanol. Geotherm. Res. (submitted on March 3, 2021).

Kanamori, H., 1977. The energy release in great earthquakes. J. Geophys. Res. 82, 2881–2987. https://doi.org/10.1029/JB082i020p02981.

Kaneda, Y., Kawaguchi, K., Araki, E., Sakuma, A., Matsumoto, H., Nakamura, T., Kamiya, S., Ariyoshi, K., Baba, T., Ohori, M., Hori, T., 2009. Dense Ocean floor Network for Earthquakes and Tsunamis (DONET) – development and data application for the mega thrust earthquakes around the Nankai trough. Am. Geophys. Union Fall Meet. Abstract ID S53A-1453.

Kawaguchi, K., Araki, E., Kaneko, S., Nishida, T., Komine, T., 2010. Subsea engineering ROV and seafloor observatory construction. Proceedings of International Symposium on Underwater Technology 2010/International Workshop on Scientific Use of Submarine Cables and Related Technologies 2010 SSC11-1019, CD-ROM.

Kennett, B.L.N., Engdahl, E.R., Buland, R., 1995. Constraints on seismic velocities in the Earth from traveltimes. Geophys. J. Int. 122, 108–124 Oxford University Press (OUP). https://doi.org/10.1111/j.1365-246x.1995.tb03540.x.

Lemoine, A., Briole, P., Bertil, D., Roullé, A., Foumelis, M., Thinon, I., Raucoules, D., de Michele, M., Valty, P., Hoste Colomer, R., 2020. The 2018–2019 seismo-volcanic crisis east of Mayotte, Comoros islands: seismicity and ground deformation markers of an exceptional submarine eruption. Geophys. J. Int. 223, 22–44. https://doi.org/10.1093/gji/ggaa273.

Lomax, A., Michelini, A., Curtis, A., 2014. Earthquake location, direct, global-search methods. Encyclopedia of Complexity and Systems Science. Springer New York, pp. 1–33 https://doi.org/10.1007/978-3-642-27737-5_150-2.

McNamara, D.E., Buland, R.P., 2004. Ambient noise levels in the continental United States. Bull. Seismol. Soc. Am. 94 (4), 1517–1527. https://doi.org/10.1785/012003001.

McNamara, D.E., von Hillebrandt-Andrade, C., Saurel, J.-M., Huerfano, V., Lynch, L., 2016. Quantifying 10 years of improved earthquake-monitoring performance in the Caribbean region. Seismol. Res. Lett. 87 (1). https://doi.org/10.1785/0220150095.

NIED, 2019. NIED S-net. National Research Institute for Earth Science and Disaster Resilience (NIED) https://doi.org/10.17598/nied.0007.

Peterson, J., 1993. Observation and modeling of seismic background noise. U.S. Geological Survey Technical Report 93-322, pp. 1–95 https://doi.org/10.3133/ofr93322.

Saurel, J.-M., Aiken, C., Jacques, E., Lemoine, A., Crawford, W.C., Lemarchand, A., Bertil, D., 2019. High resolution onboard manual locations of Mayotte seismicity since March 2019, using local land and seafloor stations. Am. Geophys. Union Fall Meet. Abstract ID V43I-0220 https://ui.adsabs.harvard.edu/abs/2019AGUFM.V43I0220S.

Saurel, J.-M., Jacques, E., Aiken, C., Lemoine, A., Retailleau, L., Lavayssière, A., Foix, O., Laurent, A., Mercury, N., Crawford, W.C., Lemarchand, A., Daniel, R., Pelleau, P., Bès de Berc, M., Dectot, G., Bertil, D., Roulle, A., Broucke, C., Colombain, A., Besançon, S., Guyavarch, P., Kowalski, P., Roudaut, M., Battaglia, J., Bodihar, S., Bouin, M.P., Canjamale, K., Desfete, N., Dofal, A., Doubre, C., Dretzen, R., Ferrazzini, V., Fontaine, F., Géli, L., Griot, C., Grunbert, M., Guzel, E.C., Hoste-Colomer, R., Lambotte, S., Léger, F., Vergne, J., Satriano, C., Tronel, F., Van der Woerd, J., Feuillet, N., Fouquet, Y., Jorry, S., Rinnert, E., Thinon, I., 2021. Mayotte seismic crisis: building knowledge in near real-time combining land and ocean-bottom seismometers, first results. Geophys. J. Int. (submitted on February 24, 2021).

Stamps, D.S., Kreemer, C., Fernandes, R., Rajaonarison, T.A., Rambolamanana, G., 2020. Redefining East African Rift System kinematics. Geology 49 (2), 150–155. https://doi.org/10.1130/G47985.1.

Tréhu, A.M., Wilcock, W.S.D., Hilmo, R., Bodin, P., Connolly, J., Roland, E.C., Braunmiller, J., 2018. The role of the Ocean Observatories Initiative in monitoring offshore earthquake activity of the Cascadia subduction zone. Oceanography 31. https://doi.org/10.5670/oceanog.2018.116.

Wald, D.J., Quitorian, V., Heaton, T.H., Kanamoir, H., 1999. Relationships between peak ground acceleration, peak ground velocity, and modified mercalli intensity in California. Earthquake Spectra 15 (3), 557–564. https://doi.org/10.1193/1.1586058.